Heliyon 10 (2024) e23904

Contents lists available at ScienceDirect

Heliyon

journal homepage: www.cell.com/heliyon

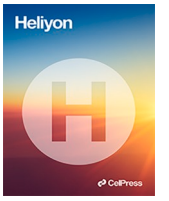

The effect of silicon microsegregation on the mechanical properties of high silicon alloyed ductile cast iron under monotonous loading

Lutz Horbach [a,*], Christian Gebhardt [a], Jiali Zhang [a], Betto David Joseph [b], Andreas Bührig-Polaczek [b], Christoph Broeckmann [a]

[a] Institute for Materials Applications in Mechanical Engineering, RWTH Aachen University, Germany
[b] Foundry Institute, RWTH Aachen University, Germany

ARTICLE INFO

Keywords:
Cast iron
Silicon microsegregation
RVE
Trace analysis
Crystal plasticity

ABSTRACT

High silicon alloyed ductile cast iron (Si-DCI) can show unpredictable brittle fracture which currently prevents a widespread application of this material. The brittleness is associated with local superstructure formation due to silicon segregation which influences the deformation mechanisms of the matrix phase. In order to understand the effect of silicon segregation on the mechanical properties of Si-DCI under monotonous loading, three alloys with different cooling conditions were examined and micromechanical simulations were carried out by using the phenomenological crystal plasticity model. Here, the segregation profiles were determined through multi phase field simulations. The influence of segregation on the mechanical properties was only evident from the model but not from the experimental results. The simulated results show that the toughness of Si-DCI decreases with stronger silicon segregation when ductile damage is considered.

1. Introduction

Due to the increasing demand for renewable energy, castings in wind turbines are becoming larger in size [1]. In order to limit their mass, these components need to endure higher stresses. Ductile cast iron (DCI) is a widely used structural material in this sector, as it offers excellent mechanical properties, good castability and low costs. Its potential can be further enhanced by solid solution strengthening with silicon. Silicon shifts the eutectoid transformation in DCI to higher temperatures, which allows a longer time for the transformation of austenite to ferrite and in turn favors the formation of ferrite instead of pearlite [2]. Several authors have shown that for alloys with silicon content between 3.2 wt% and 4.3 wt%, an increase in Si-content leads to an increase in yield limit, tensile strength and hardness [3–5]. In addition, the ratio of yield limit to tensile strength increases in this range [4]. Gonzalez et al. [6,7] observed that for cast iron specimens with high Si content around 5.2 wt% to 5.4 wt%, the yield strength and tensile strength are almost identical. However, Si-DCI can show brittle fracture depending on temperature and loading [8]. The elongation at fracture shows an inverse trend to both yield limit and tensile strength, dropping rapidly when the silicon content is above 4.3 wt% [3–7].

* Corresponding author.
E-mail addresses: l.horbach@iwm.rwth-aachen.de (L. Horbach), c.gebhardt@iwm.rwth-aachen.de (C. Gebhardt), j.zhang@iwm.rwth-aachen.de (J. Zhang), b.david-joseph@gi.rwth-aachen.de (B.D. Joseph), office.buehrig-polaczek@gi.rwth-aachen.de (A. Bührig-Polaczek), c.broeckmann@iwm.rwth-aachen.de (C. Broeckmann).

https://doi.org/10.1016/j.heliyon.2023.e23904
Received 6 September 2023; Received in revised form 6 November 2023; Accepted 15 December 2023
Available online 20 December 2023

This effect can be understood based on the principles of metal physics. Silicon atoms segregate during the solidification of Si-DCI [9]. Since the diffusion time is too short to homogenize the segregation profile, high Si contents remain in the vicinity of the graphite and decrease towards the interstices of the graphite. The silicon segregation profile is strongly dependent on the cooling rate and the density of the graphite nodules [10]. Silicon occupies lattice sites in iron and increases strength through the effect of solid solution strengthening, i.e., dislocation slip is impeded by silicon. As a result, the critical resolved shear stress (CRSS) acting on the slip system is increased. Several authors [11,12] have investigated the influence of varying silicon contents on the deformation of ferrite single crystals. Thereby, the CRSS increases linearly with increasing silicon content in the crystal, which naturally reduces its deformability. If the silicon content increases strongly locally due to the segregations, $B2$- and DO_3 superstructures may form. According to Wittig et al. [8], these are the primary cause of hardening and embrittlement in iron-silicon alloys, because they strongly restrict dislocation cross-slip. This strengthening effect that occurs due to the superlattice dislocations is particularly noticeable in the case of body-centered cubic metals, since they usually have a high tendency to dislocation cross-slip [13]. The effect of suppressing dislocation cross-slip was reported by Wittig et al. [8] in iron-silicon alloys at silicon contents above 4 wt%. They found that the resulting slip traces in alloys with Si content below 4 wt% were wavy, indicating the existence of dislocation cross-slip, while the slip traces found in alloys with above 4 wt% silicon were almost perfectly straight, i.e., planar slip [8].

Promising approaches exist to manipulate the segregation profile, as indicated by Franzen et al. [9], and thereby tailoring the mechanical properties of Si-DCI. However, only little in-depth experimental studies of the influence of the Si-segregation profile on the mechanical properties of Si-DCI were published in the literature [14]. This is probably related to the strong heterogeneity of the microstructure which leads to the interplay of multiple factors that influence the mechanical properties [15,16].

By using model-based analysis on the basis of the representative volume elements (RVE), the influences of different factors could be separated, so that a more in-depth investigation of the Si-segregation profile would be possible. Micromechanical models have been reported in 2D and 3D for DCI, often modeling the metallic matrix of the GJS microstructure as homogeneous and isotropic. Micro-segregations based on Scheil calculations in ferrite have been used in the model by Andriollo et al. [17]. In which different material properties were assigned to individual integration points, depending on the local Si-contents present in the microstructure. However, in the work of Andriollo et al. [17] only small strains and no damage were taken into account, therefore ultimately little influence of the microsegregation on the mechanical properties of Si-DCI was found.

Compared to isotropic continuum mechanical models, crystal plasticity (CP) models consider the underlying physics of crystal deformation. The classical CP-models are based on the multiplicative decomposition of the deformation gradient [18]. The tensor formulation allows to account for the deformation mechanisms of the single crystal in the constitutive law which connects the stress and deformation tensor. Recently, most physically based CP-models also account for microscopic quantities such as dislocation densities, which require the implementation of scale transition like parameters or fitting parameters [19]. This makes them not strongly distinguished from the phenomenological models any more. And the latter have also proven themselves in the efficient modeling of polycrystal deformation. CP-models have often been used for steels [20,21]. However, only little preliminary work was reported on cast iron [22], which may be attributed to their high microstructural heterogeneity and casting defects, which render consideration of crystal deformation irrelevant. However, if microsegregation is to be investigated, the CRSS acting on the individual slip system change [11,12] and thus crystal plasticity models are expected to incorporate these effects.

Multiphase field simulations offer a powerful method to locally determine the evolution of microstructure based on different cooling conditions and alloying compositions. Eiken et al. [10] have already proven their capability of phase field simulations to accurately predict silicon and manganese segregation in the microstructure of Si-GJS by comparing simulated segregation profiles calculated by using Micress Software [23,24] with ones obtained by means of experimental segregation analysis. Chen et al. [25] were able to accurately predict niobium segregation in an Inconel 718 alloy produced by laser powder bed fusion using the same software.

A coupled approach of CP calculations with phase field simulations could significantly contribute to an overall understanding of the connection between process control, alloy composition, and resulting mechanical properties. Several works have already successfully integrated this approach to achieve direct linkage between the microstructure prediction and the determination of the resulting mechanical properties. Agius et al. [26] combined both methods to generate a digital twin of the process chain of additively manufactured microstructures of Ti-5553 alloys. Thereby, the phase field simulation results may be directly transferred to the local model parameters of the CP simulation if the same mesh is utilized [26]. Pinomaa et al. [27] simulated the microstructural evolution of the 316 L stainless steel produced by selective laser melting using phase field simulation explicitly accounting for microsegregation of the solute atoms. Subsequent CP simulations were then used to predict the homogenized mechanical properties based on the simulated microstructure. Furthermore, this approach was also used for the prediction of damage. For instance, the open-source CP framework DAMASK [19], which was also used for the CP-FEM calculations in this study, provides pre-implemented conservation laws to account for phase field damage.

The major challenge in employing CP-models lies in providing the model parameters that change locally in the micromechanical model. A wide variety of possible methods to calibrate the model parameters in general were reported in the literature. Inverse methods compare either the results of experiments, such as nanoindentation [28,29] and tensile tests [30], or, in the case of full-field methods, strain fields measured by means of digital image correlation [3]. Since inverse methods are often based on some form of mathematical optimization, opening the parameter space in the present application prevents its solution. However, model parameters can also be determined directly, for example, by testing model alloys or carrying out micromechanical experiments, such as micropillar compression tests [31]. The disadvantage herein results from the high experimental effort for a continuous modeling of segregation. In an alternative approach, the required model parameters, i.e., the CRSS [11], can be determined semi-analytically using empirical data. These data are often based on fundamental studies on single crystals with different contents of the solid solution strengthening alloying element of interest. The accuracy of the simulation may then evaluated by the comparison with the experiment [20] or full-field data

[28]. Due to these challenges in deriving continuous model parameters that depend on local silicon concentration, no attempt has yet been undertaken to study the effect of silicon microsegregation on the mechanical properties of Si-DCI under monotonous loading. However, in contrast to an experimental approach the influencing factors may clearly be separated on the model level. Therefore, this paper addresses the issues by studying 3D micromechanical models that consider silicon microsegregation, which is derived from multi phase field simulations. The phenomenological crystal plasticity model was employed and its parameters, which are calibrated according to fundamental empirical research from the literature, vary locally depending on the silicon contents. The results were then compared to experimental results from tensile tests.

2. Material and methods

2.1. Material

Raw materials to produce melt include recirculation material, pure iron and ferrosilicon (FeSi). These raw materials were prepared and melted in a 50 kg medium-frequency induction furnace using a graphite crucible. After melting all raw materials at 1450 °C, the melt was overheated to 1550 °C and held at this temperature for about 5 min in order to remove impurities. After deslagging of the melt, magnesium treatment with a cerium-free magnesium master alloy at about 1430 °C was performed using a plunger. Afterwards inoculation was carried out with 0.3 wt% of an inoculant based on bismuth and cerium as nucleating agents. Samples for thermal analysis as well as spectrometric analyses were produced and the melt was cast at 1350 °C. Castings were done in Furan based sand mould with each mould containing Y2 (module: 10 mm), Y4 (module: 17 mm) standard test blocks and an insulated cylindrical sample with a diameter of 13 cm (module: 30 cm) as illustrated in Fig. 1. The mould geometry has a significant influence on the cooling rate of the casted components. The highest cooling rate was reached for the Y2 geometry, and the lowest cooling rate for the cylindrical shaped mould. In addition to the different mould geometries, the chemical compositions of the casted components were also varied. In total nine groups of materials were investigated, each group was a certain combination of a chemical composition and a cooling rate. Detailed information about the chemical compositions of the investigated materials are given in Table 1.

2.2. Experimental methods

2.2.1. Optical microscopy

In order to be able to interpret the influence of the segregations correctly, the microstructure of each casted component was analyzed. To this end, metallographic samples were taken from the geometrical center of the casted components, as elucidated for Y2, Y4 and Cyl in Fig. 1. The metallographic samples were ground and polished according to the preparation steps listed in Table 6. For each sample, more than ten images were recorded at 100× magnification with a resolution of 2600× 2060 pixels with an optical microscope. According to DIN EN ISO 945–4 [32] at least 500 graphite nodules were captured and analyzed to determine the nodularity, the Feret diameter, the circularity as well as the nodule density. The nodularity is defined as the percentage of spheroidal graphite and was determined according to the standard ASTM E2567 [33].

2.2.2. Macroscopic tensile tests and hardness measurements

In order to characterize the mechanical properties, tensile tests and Brinell hardness measurements were carried out. For each alloy and cooling rate three specimen of type B with a diameter of 10 mm were prepared according to the standard DIN-50125 [34]. The tensile tests were loaded strain rate controlled under quasi-static conditions with an overall strain rate of 0.002 1/s and the ultimate tensile strength (UTS), the 0.2 % offset yield limit ($\sigma_{Y0.2}$), as well as the elongation at fracture (A) were calculated. The Brinell hardness was determined according to DIN EN ISO 6506 [35] with a ball diameter of 2.5 mm and a load of 187.5 N.

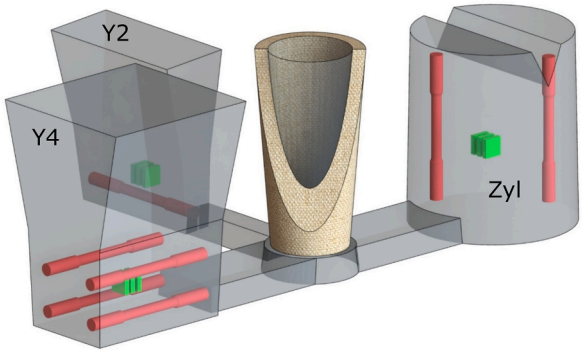

Fig. 1. Visualization of the different moulding geometries and casting of Y2, Y4 and Cyl samples. (green: metallographic samples, red: tensile samples). (For interpretation of the references to color in this figure legend, the reader is referred to the Web version of this article.)

Table 1
Chemical composition of the investigated alloys.

Alloy	*C* [wt.%]	*Si* [wt.%]	*Sc* [wt.%]	*Mn* [wt.%]	*Mg* [wt.%]
HighSi	3.08	4.30	1.05	0.15	0.04–0.06
MediumSi	3.25	3.80	1.05	0.15	0.04–0.06
LowSi	3.58	2.80	1.05	0.15	0.04–0.06

2.2.3. Scanning electron microscopy

SEM analysis was performed on an EDAX/TSL system (AMETEK GmbH, Weiterstadt, Germany) equipped with a Hikari camera in a FEI Helios Nanolab G3 CX DualBeam (Thermofisher GmbH, Dreieich, Germany). The metallographic samples were analyzed by electron backscatter diffraction (EBSD) in order to measure the grain size distribution of the metallic matrix. Large area EBSD scans over 1000 µm × 500 µm in size that could provide sufficient statistics on the ferritic grains were conducted at 20 kV and 5.5 nA with a step size of 500 nm. The obtained data include location parameter μ and shape parameter σ of a logarithmic normal distribution describing the grain size distribution (cf. Eqn. (9)), as well as the average grain sizes and the standard deviations. Additional energy dispersive x-ray spectroscopy (EDS) mappings were carried out at 20 kV and 2.8 nA in order to determine the silicon distribution on the sample surface of the investigated samples.

2.2.4. EBSD-assisted trace analysis and in-situ tensile tests

The samples for the combined in-situ and trace analysis were also machined out of the geometrical center of each mould (Y2, Y4 and Cyl). The technical drawing of the sample geometry used is given in Fig. 2. All samples were ground manually in several steps with SiC papers, with a successively finer granulation from 80 to 1200. After grinding, the samples were polished (see preparation plan in Table 6 in the appendix). All in-situ tensile tests were performed on a Kammrath and Weiss in situ tensile tester, with an overall strain rate of 0.002 1/s. The in-situ observation was performed on a Tescan Clara FE-SEM, all tests were interrupted during the microstructural analysis. In order to compare the deformation and damage mechanisms under tensile loading between samples of different silicon content, electron microscopy analyses were carried out at different loading points during the tensile test. EBSD scans of the region of interest (ROI) were then used to carry out the slip trace analysis.

The EBSD-assisted trace analysis is a widely used method to analyze the deformation mechanism and the activation of slip systems due to an external loading [36,37]. Extensive studies were already carried out on the deformation mechanisms of pure ferrite, which showed the possibility of activating various slip systems depending on loading conditions and temperature, such as {110}⟨111⟩, {112}⟨111⟩, {123}⟨111⟩, as well as slip on non-crystallographic orientations [13,38]. Recent studies of Caillard [39,40] showed, that the elementary slip systems of pure ferrite at room-temperature are the {110}⟨111⟩ systems accompanied by extensive cross-slip. Based on the findings of Caillard [39,40], the slip trace analysis performed was intended to clarify whether the amount of silicon soluted in the ferritic matrix affects the elementary slip systems.

In order to decrease the experimental effort, only three samples of the alloy HighSi with 4.3 wt% silicon were investigated, since the influence of silicon content on the deformation mechanisms is expected to be most pronounced on samples of the highest silicon content. The evaluation of activated slip systems under the investigated loading conditions was carried out as follows. Dislocations glide on slip planes and form steps with the height of one Burgers vector on the sample surface, when they leave the sample. The visible surface steps seen on micrographs, which are normally referred to as slip bands, are formed by a large number of dislocations. As the dislocations only glide on the activated slip planes, they appear as parallel lines along the slip plane traces which are the intersecting lines between the slip plane and the sample surface. Following this, the activated slip systems can be identified by finding the match between the slip bands and the slip plane traces that are obtained from the orientation measurement by EBSD.

Based on the symmetry of the bcc-lattice, the numbers of the slip plane traces which are detectable by 2D analyzing methods, are 6, 12 and 24 for the {110}-, {112}- and {123}-plane families. Due to the increasing possibility of finding a match between slip plane trace and slip bands with increasing number of non-parallel slip planes in a slip system family, all slip bands found on the sample surfaces were first checked for parallelism to the {110}-slip planes. In cases where parallelism could not be detected, local postmortem EBSD measurements were performed to clarify the reason for the misorientation between slip bands and {110}-slip plane traces.

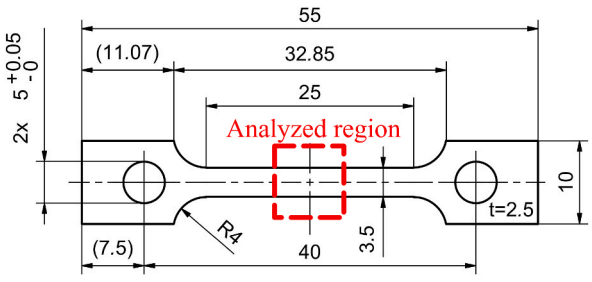

Fig. 2. Technical drawing of the specimen for the slip trace analysis and the in-situ tensile tests.

2.3. Simulation methods

In order to understand the influence of the segregation on the mechanical properties, a simulation chain was implemented. In a first step, experimentally calibrated multi-phase field simulations were performed. The microstructure and the local silicon concentrations were subsequently passed to the micromechanical simulation, where a phenomenological crystal plasticity law was used to determine the homogenized stress-strain curve.

2.3.1. Multi-phase field simulation

The simulations of the solidification were performed by using Micress Software [23,24] and the thermodynamic data were carried over through GES files developed from Thermocalc [41]. In Micress, multiple phases were defined in terms of different phase field variables $\varphi_\alpha(\mathbf{x},t)$, where the indices α, β and γ represents either the liquid phase (L), the austenite phase (γ) or the graphite phase (G). The simulations were carried out over 3D cubic domains with each side having a length of 100 μm and a grid spacing of 2 μm, which was chosen based on the results of a preliminary sensitivity study revealing that an increase in spacing from 1 μm to 2 μm has no significant effect on the results of the phase field simulation. The underlying phase field equation reads as follows

$$\dot{\varphi}_\alpha(\boldsymbol{x},t) = \sum_\beta M^\varphi_{\alpha\beta}\left(\left|\nabla\varphi_{\alpha\beta}\right|\nu^{-1}_{mol,\alpha\beta}\Delta\mu_{\alpha\beta} - \sigma_{\alpha\beta}K_{\alpha\beta} + \sum_\gamma J_{\alpha\beta\gamma}\right), \tag{1}$$

where $M^\varphi_{\alpha\beta}$ denotes the interfacial mobility based on diffusion-controlled limits, $\Delta\mu_{\alpha\beta}$ denotes the difference in chemical potential and $\nu_{\mathrm{mol},\alpha\beta}$ is the mean molar volume for interacting phases α and β. The second term in the brackets of equation (1) corresponds to the capillary forces, with $\sigma_{\alpha\beta}$ as the interfacial energy and $K_{\alpha\beta}$ as the pairwise curvature. Furthermore, the third term $J_{\alpha\beta\gamma}$ is a higher order term denoting the junction forces at the triple junctions of α, β and γ. Moreover, the spheroidal graphite was modeled by effective anisotropy functions and 25 irregularly arranged facets [42]. The local concentration of the alloying elements carbon and silicon in terms of mole fractions are given by composition vector fields represented by $\chi(\mathbf{x},t)$. The diffusion of these alloying elements through different phases were simulated based on phase specific diffusion matrices $\mathbf{D}_\alpha$. The formulation of the diffusion equation follows as

$$\dot{\boldsymbol{\chi}}(\boldsymbol{x},t) = n^{-1}_{mol}(\boldsymbol{x},t)\sum_\alpha \nabla\cdot\left[n_{mol}(\boldsymbol{x},t)\boldsymbol{D}_\alpha\nabla_{\chi_\alpha}\right], \tag{2}$$

allowing for locally changing mole number densities $n_{\mathrm{mol}}(\mathbf{x},t)$, which are not affected by substitutional diffusion, but change during interstitial diffusion of carbon (C), such that

$$\dot{n}_{mol} = f\left(\dot{\chi}^C_\gamma\right). \tag{3}$$

Furthermore, a volumetric relaxation approach was taken into consideration for the homogeneous volume expansion.

The phase field simulations were carried out for the three different alloy compositions, which are listed in Table 1 and for different cooling conditions, for which the heat extractions defined by the mould geometries. The corresponding heat flows are −7.50 J/(scm^3), −0.782 J/(scm^3) and −0.672 J/(scm^3) for the Y2-, the Y4- and the Cyl-mould, respectively. The temperature evolution, which was homogenously assigned to the RVE domain, was enforced to replicate the experimental cooling curves of the Y2, Y4-, and cylindrical samples. Fig. 3, shows the experimentally obtained cooling curves from an initial temperature of approximately 1230 °C to a final temperature of approximately 752 °C which corresponds to the onset of the eutectoid transformation. At first, the nucleation of primary austenite from the liquid phase takes place followed by its dendritic growth, then graphite nodules nucleate continuously at random positions in the melt, and they get encapsulated by either the primary austenite or the formed eutectic austenite. The further growth of graphite depends on the interstitial diffusion of carbon in austenite. The initial nucleation temperatures of primary austenite,

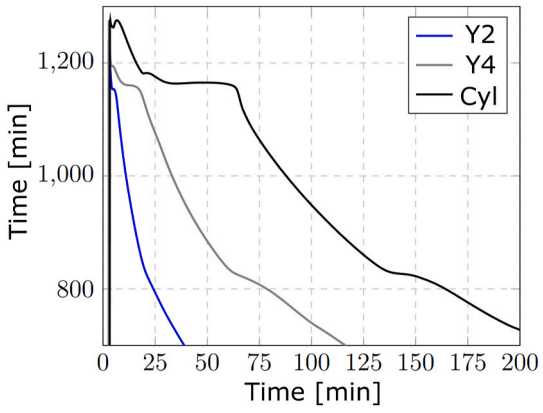

Fig. 3. Experimentally measured cooling curves of the Y2-, Y4- and cylindrical mould geometry.

graphite and eutectic austenite vary based on the cooling conditions and alloy compositions. It is important to note that all simulations were terminated prior to the eutectoid transformation. However, the assumption of a final temperature of 752 °C is still reasonable, as Eiken et al. [10] have already shown that the silicon profile of the completely solidified austenitic microstructure does not differ significantly from that at room temperature. Fig. 4 illustrates the different progress of solidification depending on the cooling rate which is determined by the mould geometry.

2.3.2. Constitutive material model

The phenomenological crystal plasticity (CP) model, which is incorporated in the DAMASK framework [18,19] was used to model the plastic deformation of the ferrite in the DCI microstructure. The CP model is based on the formulation of Hutchinson [43] and was modified for bcc-crystals. Thereby, dislocation slip is initiated, when the resolved shear stress τ^{α} of a certain slip system α exceeds the CRSS τ_c^{α}. When dislocation slip takes place, the shear rate $\dot{\gamma}^{\alpha}$ of the corresponding slip system increases according to

$$\dot{\gamma}^{\alpha} = \dot{\gamma}_0 \left| \frac{\tau^{\alpha}}{\tau_c^{\alpha}} \right|^n sgn(\tau^{\alpha}), \tag{4}$$

leading to an accumulation of plastic deformation. In Eq. (4), $\dot{\gamma}_0$ represents the reference shear rate and n is referred to as stress exponent. As a result of dislocation interaction, the CRSS increases towards its saturation stress τ_s. The evaluation of the CRSS is described by

$$\dot{\tau}_c^{\alpha} = \sum_{b=1}^{N} \dot{\gamma}^b h_0 \left| 1 - \frac{\tau_c^b}{\tau_s} \right|^w sgn\left(1 - \frac{\tau_c^b}{\tau_s} \right) q_{ab}, \tag{5}$$

where N represents the total number of considered slip systems, h_0 and w are fitting parameters and q_{ab} are coefficients of the interaction matrix which takes into account the anisotropy of hardening. For co-planar slip, q_{ab} takes the value 1.0, else it is 1.4. Although it is well known that the graphite nodules in the DCI microstructure exhibit high anisotropy due to their internal structure and that this significantly affect the prediction accuracy of the model [44,45], they were modeled in this work as purely elastic and isotropic, with a Young's Modulus of 30 GPa and a Poisson's ratio of 0.3. This assumption was employed here to save computational power, since the focus of the study is to investigate the influence of silicon segregation on the homogenized mechanical properties under monotonous loading, which is done by a direct comparison between models with and without segregations.

The damage was modeled using a simple isotropic damage formulation for ductile materials, which was already implemented in version 2.03 of the CP framework DAMASK. Similar to the selection of the CP model, the simplistic strain-based formulation was used here to gain the first understanding of the effect of silicon segregation on damage as well as to avoid time-consuming parameter determination phase for more complex damage models. In addition, Qayyum et al. [46,47] have successfully applied this model to study the damage initiation and evolution in transformation induced plasticity steels and dual phase steels. Therefore, it is believed that this simple model is the best suited at the current stage of the study. Thereby, the damage initiates, when the accumulated plastic deformation exceeds the critical value γ_{crit}.

$$\Phi = \min\left(1, \frac{\gamma_{crit}}{\sum_{\alpha=1}^{N} \gamma^{\alpha}} \right) \tag{6}$$

According to Roters et al. [18,19], the damage parameter Φ was introduced only into the elastic part to successively reduce the effective elastic stiffness C_{eff} of the damaged elements following:

$$C_{eff} = (1 - \Phi)C. \tag{7}$$

For damage free elements, Φ becomes 1, and in case of already damaged elements, it is less than 1. For each element the second Piola-Kirchhoff stress **S** is calculated as a function of the effective elastic stiffness and the Green-Lagrange strain **E** according to a generalized Hook's law:

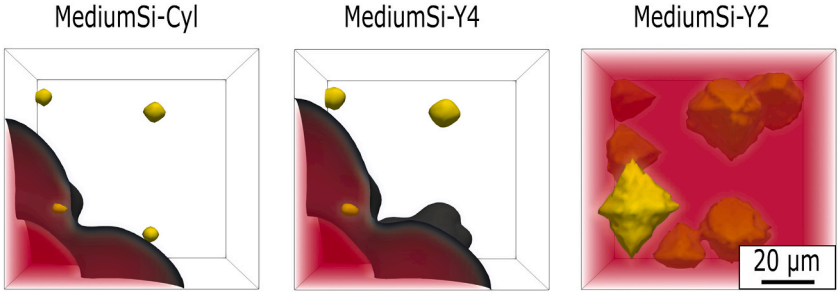

Fig. 4. Comparison of the growth progress of austenite (red) and graphite (yellow) between the different mould geometries of the alloy MediumSi 84 s after the start of solidification. (For interpretation of the references to color in this figure legend, the reader is referred to the Web version of this article.)

$$\boldsymbol{S} = C_{eff}\boldsymbol{E}. \tag{8}$$

Subsequent update of the slip rates of each slip system ensures the accumulation of plastic strain in already damaged elements with ongoing deformation, whereby damage can propagate, if the resolved shear stress again exceeds the CRSS. It was assumed that relevant damage occurs only in the ferrite phase which is considered to be justified since the debonding between the graphite nodules and the ferrite phase starts at an early stage of deformation and the damage leading to a macroscopic failure of the DCI structure is characterized by large accumulation of plastic deformation in the ferritic matrix [44,48,49]. The interface between graphite nodules and ferrite matrix is modeled as ideal, i.e., possible debonding is not considered in the models in this work. It has been confirmed by the literature [50–52] that perfectly bonded graphite nodules hinder the lateral contraction of the surrounded matrix perpendicular to the principal direction of straining, which leads to an overestimation of strength. However, considering the great difficulty in local parametrization and the resulted complexity of the model, the implementation of weak interfaces will be beyond the scope of the work of gaining the first understanding of the effect of silicon segregation. Therefore, the setting of an ideal interface is justified, when the simulation results of models with and without segregation are only cross compared with each other within the work. In order to investigate the influence of silicon segregations on mechanical properties of DCI under monotonic load, the CRSS, τ_s, as well as γ_{crit} were determined as functions of the local silicon content. Their determination was based on the results of the macroscopic tensile tests and is therefore described in Section 3.4. The remaining material properties for the ferrite phase were taken from the literature [28] and kept constant (see Table 2).

2.3.3. RVE model generation

The multi-phase field simulations provide a continuous distribution of the local silicon, as well as the graphite morphology over the entire RVE domain as functions of the chemical composition and the cooling rate. The obtained distribution of silicon was then uniformly discretized. In a next step, the model parameters, which were assumed to be locally dependent on the amount of silicon were assigned to these regions. Fig. 5 exemplary shows the resulting discrete distribution of the silicon weight fraction over the domain of the model for MediumSi-Y4.

Since the phase field simulations were only performed until the start of the eutectoid transformation, the austenite-ferrite transformation was not incorporated. A voronoi-algorithm [53–55] was used to generate a statistically equivalent artificial grain structure for each model, which was based on the determined grain size distributions represented by a two parameter logarithmic normal distribution, with a probability density function defined as follows

$$p(x) = \frac{1}{x\sigma\sqrt{2\pi}}\exp\left(-\frac{(ln(x)-\mu)^2}{2\sigma^2}\right). \tag{9}$$

The values of the location parameter μ and the shape parameter σ are given in Table 4 for each sample.

On the one hand, although the grain size distribution graphs obtained by large EBSD scans show close agreement among all samples, they still give different fitting parameters. On the other hand, the RVE used in this study has a relatively small size which does not allow the best representation of the real grain size distribution of a sample. Therefore, it was decided to apply a logarithmic normal distribution with respect to the EBSD average grain size value of each sample (cf. Table 4) in the corresponding RVE. The generated models were solved by the spectral solver incorporated in the crystal plasticity framework DAMASK [19]. A structured mesh of cubic elements was used for all RVE-models with an element edge length of 2 μm. Periodic boundary conditions were employed and the RVE-models were loaded with a strain rate of 0.002 1/s defined by a uniaxial rate of the overall deformation gradient. The results were then homogenized by a numerical homogenization scheme, in order to obtain the stress-strain curve from which the yield limit, the tensile strength and the elongation at fracture were then determined. Here, the microscopic stress and strain fields were volumetrically averaged over the RVE domain. Furthermore, the toughness (U), which is defined as the strainenergy-density at the moment of macroscopic fracture, was determined by numerical integration of the stress-strain curve.

3. Results

3.1. Pristine microstructure

The pristine microstructure of the castings is characterized by their graphite morphology and the grain size distribution of the

Table 2
Material properties of pure ferrite not depending on the local silicon content [28].

Property	Value	Unit
C_{11}	233.3	GPa
C_{12}	235.5	GPa
C_{44}	128.0	GPa
$\dot{\gamma}_0$	0.001	[1/s]
h_0	1000	GPa
n	20	[−]
w	2.25	[−]

Table 3
Quantitative graphite nodule analysis.

Sample	$\overline{D}_{Feret}$ [μm]	Nodularity [%]	Mean Circularity [−]	Nodule density [1/mm^2]
HighSi-Y2	19.9	90.5	0.78	338.2
HighSi-Y4	23.1	86.5	0.74	272.6
HighSi-Cyl	31.1	74.1	0.68	156.1
MediumSi-Y2	22.9	86.0	0.75	275.8
MediumSi-Y4	18.8	90.2	0.77	172.1
MediumSi-Cyl	36.0	73.6	0.68	135.7
LowSi-Y2	25.9	85.3	0.74	235.6
LowSi-Y4	31.4	85.9	0.71	164.9
LowSi-Cyl	43.2	65.6	0.63	83.9

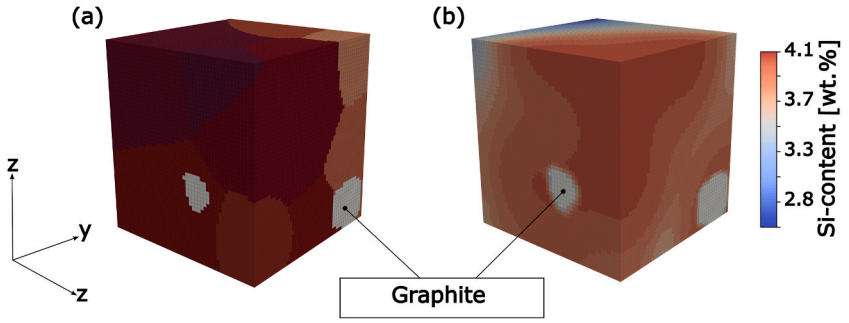

Fig. 5. Visualization of the grain structure (a) and the discrete silicon distribution (b) in the RVE-model MediumSi-Y4. The legend only belongs to the silicon distribution. (For interpretation of the references to color in this figure legend, the reader is referred to the Web version of this article.)

Table 4
Location parameter (μ) and shape parameter (σ) of a two-parameter logarithmic normal distribution, average grain size and standard deviation determined by large area EBSD scans.

Sample	μ	β	Average grain size [μm]	St. Dev. [μm]
HighSi-Y2	4.082	0.5692	67.67	30.85
HighSi-Y4	3.857	0.4739	51.98	20.30
HighSi-Cyl	3.862	0.5130	53.11	22.72
MediumSi-Y2	3.617	0.5715	42.50	19.63
MediumSi-Y4	3.964	0.5599	59.88	27.32
MediumSi-Cyl	3.972	0.5205	59.57	26.38
LowSi-Y2	3.523	0.6380	39.62	19.41
LowSi-Y4	3.783	0.5838	50.25	22.92
LowSi-Cyl	3.764	05687	49.37	23.30

ferritic matrix. The graphite morphology was analyzed by optical microscopy. The results in Table 3 show an increased nodule density for the casting geometries Y2 and Y4 compared to the material with slower cooling rate in Cyl for all of the investigated compositions. This leads to the respective differences in size of the graphite nodules characterized by the Feret diameter. Comparing the same cooling rate but different composition, cooling rates Y2 and Cyl show increasing Feret-Diameters with decreasing global silicon content. However, both cooling rate and silicon content seem to affect the graphite morphology, which is reflected by the nodularity as well as

Table 5
Averaged mechanical properties of the investigated specimen, standard deviation in brackets.

Sample	$\sigma_{Y0.2}$ [MPa]	UTS [MPa]	A [%]	$HB_{2.5/187.5}$
HighSi-Y2	534.5 (10.4)	654.1 (2.7)	13.5 (0.8)	231.7 (4.7)
HighSi-Y4	534.6 (1.1)	651.1 (1.9)	13.8 (0.5)	230.7 (4.3)
HighSi-Cyl	526.7 (7.1)	634.5 (5.4)	7.5 (1.0)	228.7 (5.0)
MediumSi-Y2	408.4 (3.9)	521.5 (1.6)	17.3 (0.7)	182.7 (4.6)
MediumSi-Y4	403.2 (3.9)	515.3 (1.9)	18.2 (0.4)	184.6 (4.8)
MediumSi-Cyl	403.9 (1.9)	500.7 (1.8)	10.9 (1.1)	181.4 (5.4)
LowSi-Y2	348.5 (0.6)	471.7 (3.8)	20.2 (0.5)	165.8 (5.2)
LowSi-Y4	345.3 (6.6)	467.9 (11.5)	19.5 (1.4)	163.8 (6.2)
LowSi-Cyl	335.4 (2.4)	450.8 (3.9)	13.4 (2.0)	158.1 (7.0)

the mean circularity of the graphite nodules. The nodularity represents the fraction of spheroidal graphite nodules defined by the aspect ratio according to ASTM-E2567 [33]. Generally, large cooling rates lead to larger nodularity and the nodularity surprisingly increases following the increase of the silicon content. Table 4 clearly shows no significant different between the grain size distributions of the various cooling rates and alloy compositions.

3.2. Macroscopic tensile tests and hardness measurements

Table 5 shows the averaged results of the tensile tests and hardness measurements, where the corresponding standard deviations are given in brackets. As the results show, $\sigma_{Y0.2}$ and UTS increase with increasing silicon content, whereby the elongation at break *A* shows an inverse trend. In the same manner as the strength, also the values of Brinell hardness decrease with decreasing amount of silicon soluted in the ferritic matrix of the DCI. The alloy with the highest silicon content is characterized by the highest hardness.

3.3. EBSD-assisted trace analysis and in-situ tensile tests

The orientations of 50 sets of slip bands in different grains of the investigated samples (cf. Fig. 2) were analyzed. The results show that 48 sets of slip bands were parallel to the {110} slip plane traces. However, two sets of the slip bands did not match the {110} slip plane traces in the respective grains. Both of these slip traces were found on sample HighSi-Cyl. Fig. 6 exemplary shows different slip traces observed on the surface of a sample of HighSi-Cyl. In order to visualize the grain orientation, the results of the corresponding EBSD measurement in the undeformed state were transparently overlaid on the SE-images. The {110} slip plane traces, which are parallel to the formed slip bands, are indicated by solid red lines. The images A and B show also the slip bands, which were not parallel to the {110} slip plane traces. The dashed red lines indicate, that parallelism to the {112} slip plane traces could be detected in both cases. Local post-mortem EBSD measurements of the regions A and B in Fig. 6 were additionally performed and the corresponding inverse pole figures of both regions are shown in Fig. 7. A direct comparison between the post-mortem EBSD images and the corresponding SE-images indicates, that in the immediate vicinity of the slip bands, which are not parallel to the {110} slip plane traces, large deformation occurred resulting in a rotation of the crystal lattice. In the case of region B, the reason for the large plastic deformation was a graphite nodule located directly under the sample surface causing the generation of a surface crack, which propagated during the tensile test and then led to a highly deformed region around the crack tip.

Additional to the trace analysis, which was only performed on samples of the composition HighSi, further in-situ analysis on samples of the alloy LowSi were performed to compare the deformation mechanisms with those of the alloy HighSi and to qualitatively verify the assumption of the damage model used. Fig. 8 exemplarily shows forescatter electron images taken during the in-situ tensile

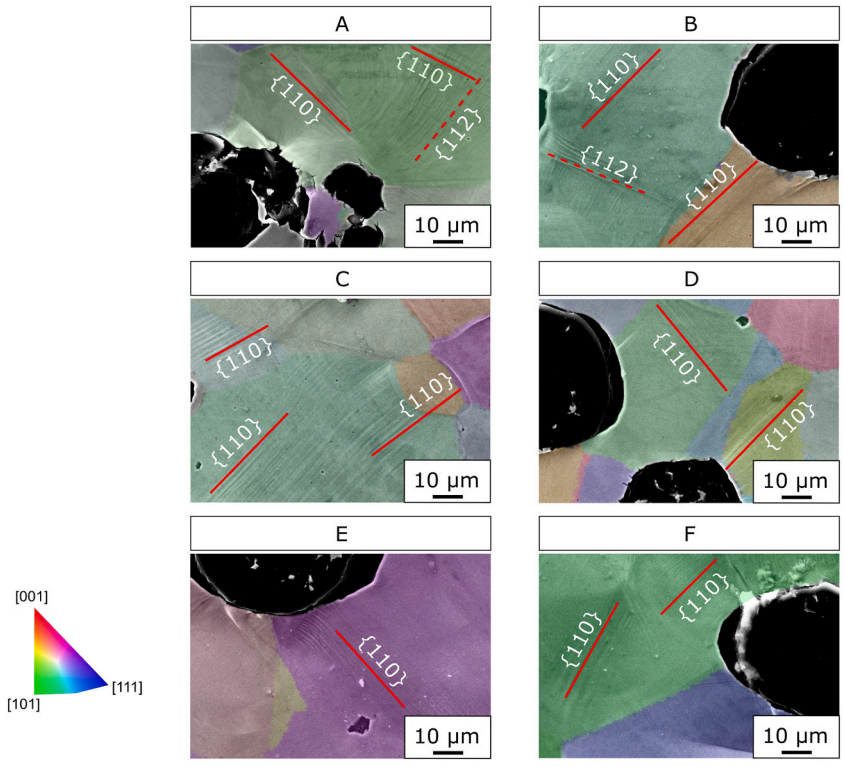

Fig. 6. Slip traces of non-parallel slip planes {110} in sample HighSi-Cyl at six different regions (A–F).

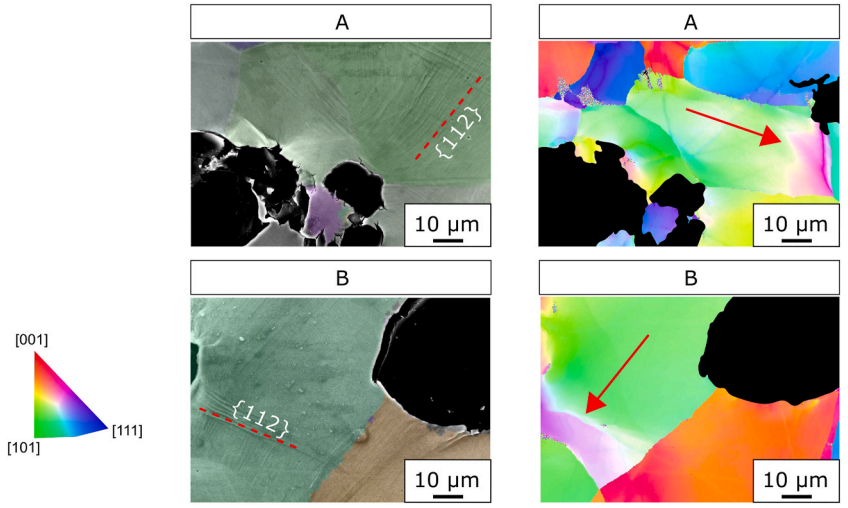

Fig. 7. Slip traces of non-parallel slip planes {110} after final failure of the sample HighSi-Cyl.

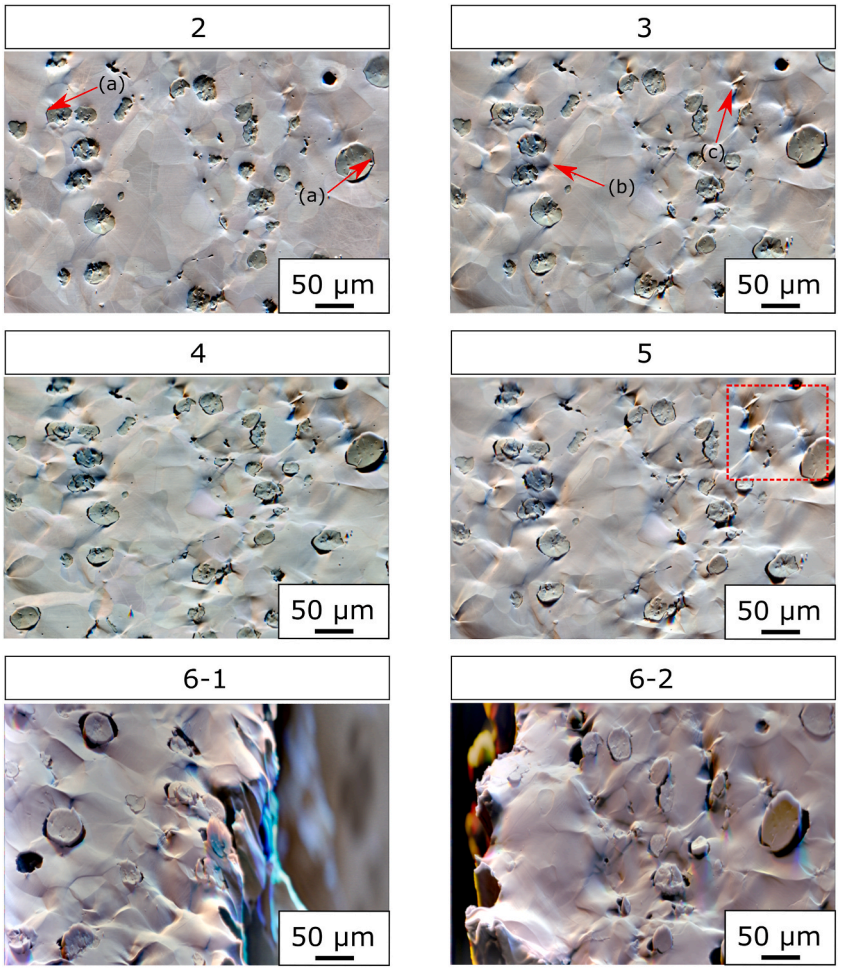

Fig. 8. Colored back-scattered electron (BSE) images of sample LowSi-Cyl during the performed in-situ tensile test at different loading points corresponding to the stress-strain curve shown in Fig. 9.

test of a sample of LowSi-Cyl. Fig. 9 shows the obtained stress-strain curve of the same sample in combination with the corresponding loading points, at which the above mentioned measurements were performed. The number above each image in Fig. 8 corresponds to the number of the loading-points marked on the stress-strain curve plotted in Fig. 9. In all in-situ tensile tests, debonding at the interface between graphite nodules and ferrite initiated immediately after exceeding the macroscopic yield limit, which can be also seen in region (a) in Fig. 8. As the deformation proceeds, the plastic deformation in the ferritic matrix increased significantly, resulting in topography changes, especially visible in the regions (b) and (c) in Fig. 8. In region (b), multiple graphite nodules are located in a close proximity to each other, resulting in the concentration of plastic deformation and thus significant change in topography. As seen from images 6–1 and 6–2 in Fig. 8, the crack, which eventually caused the macroscopic failure of the specimen LowSi-Cyl also propagated through location (b).

A SE-image of the region surrounded by the red dashed rectangle in Fig. 8 is given in Fig. 10 on the right. From this, the massive plastic deformation exhibited by the ferritic matrix during the tensile test becomes clearly visible. The SE-image in Fig. 10 was captured at load point 5 of the corresponding stress-strain curve in Fig. 9. Further, a qualitative comparison of the shape of the formed slip bands on samples with low and high silicon contents in Fig. 10 also shows, that slip bands on specimens of the alloy LowSi tended to have a wavy shape, whereas the slip bands on samples of alloy HighSi appeared as almost perfect straight lines. This is consistent with the observations of Wittig et al. [8], who observed a transition point at about 4 wt% silicon, above which the deformation mode transforms from wavy to planar slip due to the formation of $B2$- and DO_3-superstructures. The presence of superstructures and the associated formation of APB prevent dislocation cross-slip, which causes the transition to wavy slip.

3.4. Constitutive model parameters

Model parameters, in particular the CRSS, which are assumed to be locally dependent on the silicon content were determined using a combined approach, based on literature data, macroscopic tensile test results and physically based estimations. It is important to point out that based on the results of the trace analysis performed in this study, only the $\{110\}\langle 111\rangle$ slip systems were considered in the models. Kitajima et al. [11] determined the CRSS by means of single crystal tensile tests of high purity iron base alloys with different solute elements in a temperature range between 4.2 K and 300 K. Fig. 14 shows the values of the CRSS measured by Kitajima et al. [11] at 300 K and the values for the 0.2 % offset yield limit of DCI alloys as a function of the global silicon content. The linearity between CRSS and silicon content was reported by many researchers [11,12,56]. Interestingly, the macroscopic yield limits of Si-DCI shows also a linear trend, differing only by its slope from that of the CRSS values. Since data of the saturation stress τ_s (cf. Eqn. (5)), as well as of the values for the critical strain γ_{crit} were not reported in the literature, their dependence on the local silicon content was estimated and validated by comparing the simulation to the experiment.

The saturation stress is limiting the hardening of the material and is therefore considered as “microscopic tensile strength” acting on a slip system. Based on these considerations, the relation between saturation stress and macroscopic UTS were assumed to be also similar to the relation between CRSS and $\sigma_{Y0.2}$. Since the macroscopic UTS increases linearly with increasing silicon content, the saturation stress was assumed to be also linearly dependent on the soluted amount of silicon in the crystal, with a slope chosen in such a way, that the ratio between the slope of τ_s and the slope of UTS equals the ratio of the slopes of CRSS and $\sigma_{Y0.2}$. Both functions were assumed to intercept at a silicon content of 0 wt%. Fig. 15 shows the trend of the estimated values for τ_s compared to the tensile strength of DCI alloys with varying total silicon content.

An analogous procedure was used to adopt the values of critical shear γ_{crit}, which determines the onset of damage in the ferritic DCI matrix. The trend of the elongation at fracture of different cast iron grades over the global silicon content was qualitatively transferred to the trend of γ_{crit}. For this purpose, the elongations at fracture were fitted, as indicated by the dashed line in Fig. 16. However, the

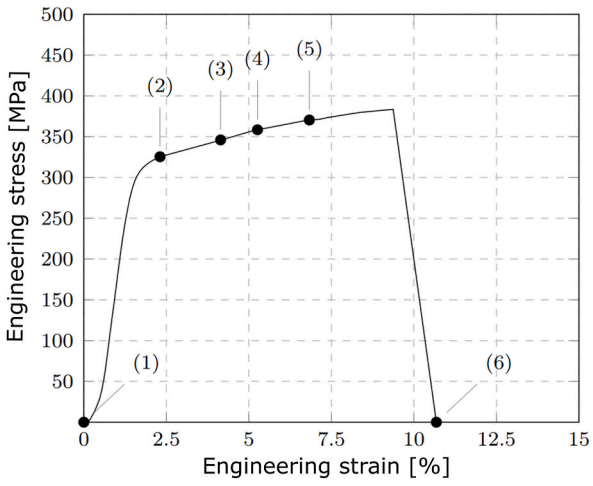

Fig. 9. Measurement points during the in-situ tensile test of sample LowSi-Cyl.

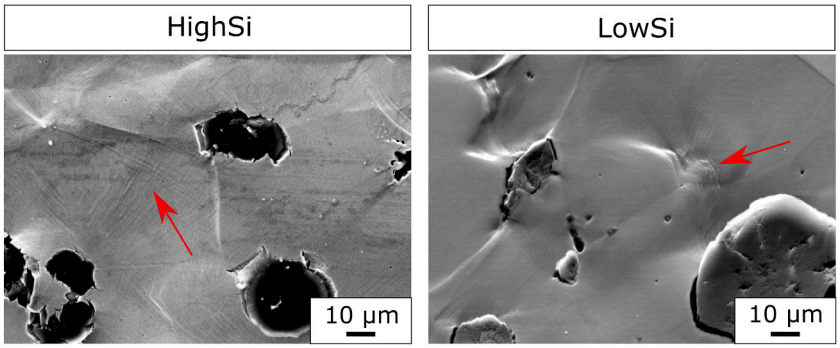

Fig. 10. Comparison of slip between slip bands of HighSi-Cyl (left) and LowSi-Cyl (right). The LowSi-Cyl shows wavy slip bands whereas the HighSi-Cyl shows straight slip bands (red arrows). (For interpretation of the references to color in this figure legend, the reader is referred to the Web version of this article.)

dependence of the critical shear below 2.8 wt% percent was assumed to be constant, because statistically reliable data is missing in this region. However, Fig. 16 shows a kink point at a silicon content of around 3.3 wt%, below which the slope of the elongation at fracture decreases with decreasing silicon content, which justifies this assumption. The resulting trend of γ_{crit} over the amount of silicon is also shown in Fig. 16.

3.5. Crystal plasticity simulations

In the following, the results of the crystal plasticity RVE simulations are presented. Fig. 11 exemplarily shows the effect of silicon segregation on the simulated stress-strain curves of the MediumSi-Y4 model, with phase field segregation profile and with a completely homogenized profile considering models with and without damage in the ferritic matrix. Generally, the silicon segregation slightly decreases the overall strength. Fig. 12 shows the equivalent plastic strain plotted over intersection planes parallel to the xz-plane at $y = 50$ µm of different RVE at a time of $t = 30$ s. Based on these plots a direct comparison between RVE with phase field segregation field and with homogenized segregation field can be made. Both cases show a nearly identical strain partitioning, which clearly explains the small difference observed in the stress-strain curve shown in Fig. 11. The black lines indicate the stress-strain curves of the same models, but without the consideration of damage in the ferritic matrix. If damage is considered in the model, the effect of silicon segregation on the strength is more pronounced and the elongation at fracture decreases due to the segregation.

The phenomenon is the same for all models simulated. Compact presentation of the results of the performed RVE simulations given in Fig. 13. In this, $\sigma_{Y0.2}$, UTS, A and U of the models with phase field segregation profile (red) and homogenized segregation profile (blue) are plotted. As the plots show, both the calculated values of 0.2 % offset yield limit and tensile strength are consistently lower for the models with phase field segregation profile compared to the models with homogenized segregation profile. However, the difference is negligible. Fig. 13 indicates that the difference in the elongation at fracture, as well as in the toughness, are higher in comparison to the difference in $\sigma_{Y0.2}$ and UTS. Furthermore, it can be clearly seen, that the models with the silicon segregation profile

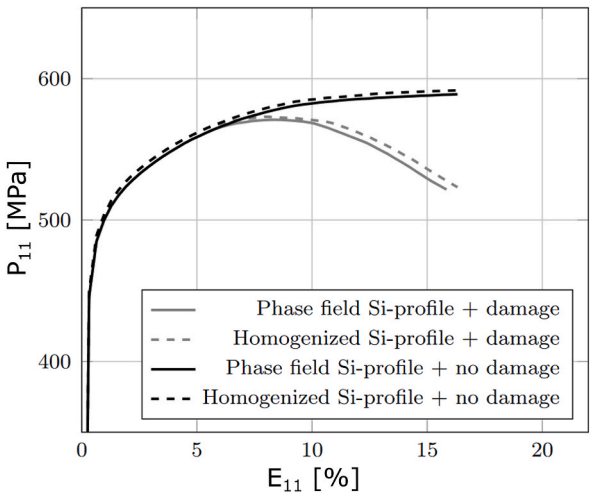

Fig. 11. Comparison of the simulated stress-strain curves of model MediumSi-Y4, with silicon segregation profile calculated by means of the phase field simulation and with homogenized segregation profile.

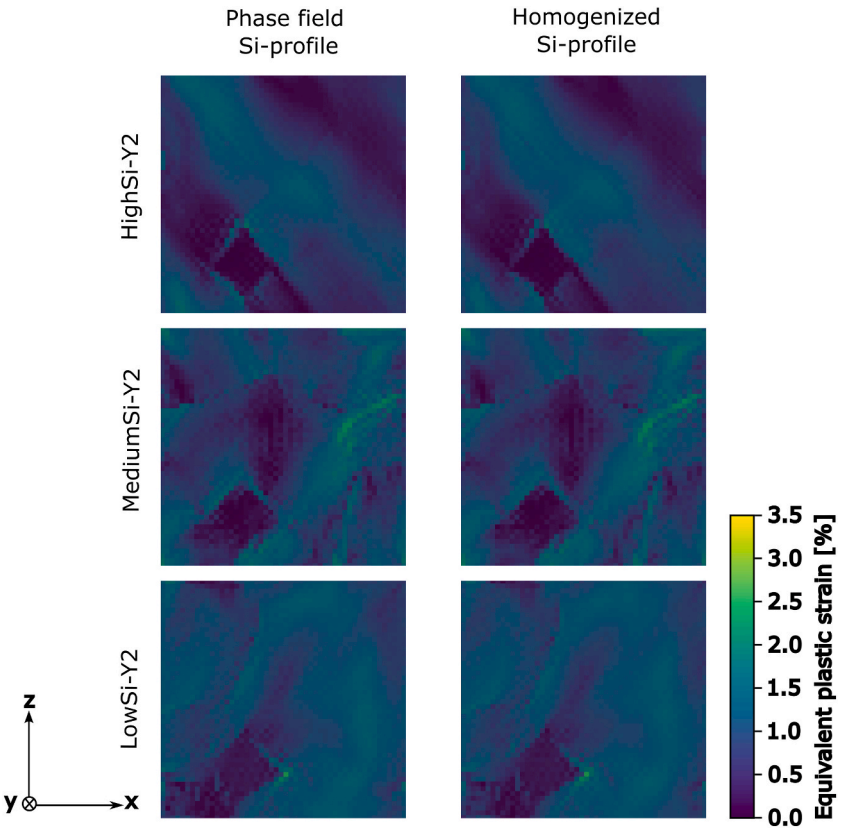

Fig. 12. Comparison of the equivalent plastic strain at a time of t = 30s between models with phase field segregation profile and homogenized segregation profile. The intersection plane is parallel to the xz-plane at y = 50 μm, with x-axis as the loading direction.

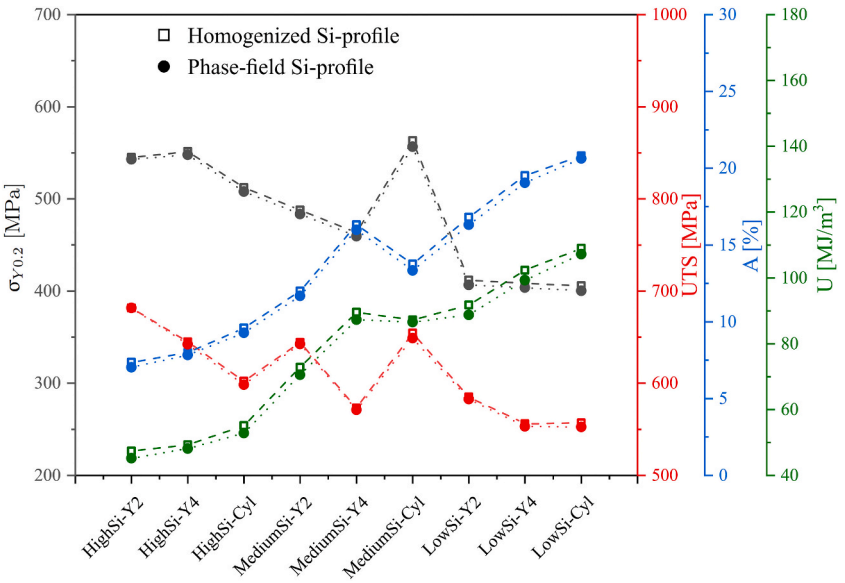

Fig. 13. Comparison of the simulated values for $\sigma_{Y\,0.2}$, UTS, A and U between the models with homogenized silicon segregation profile and silicon segregation profile from multi-phase field simulation. (For interpretation of the references to color in this figure legend, the reader is referred to the Web version of this article.)

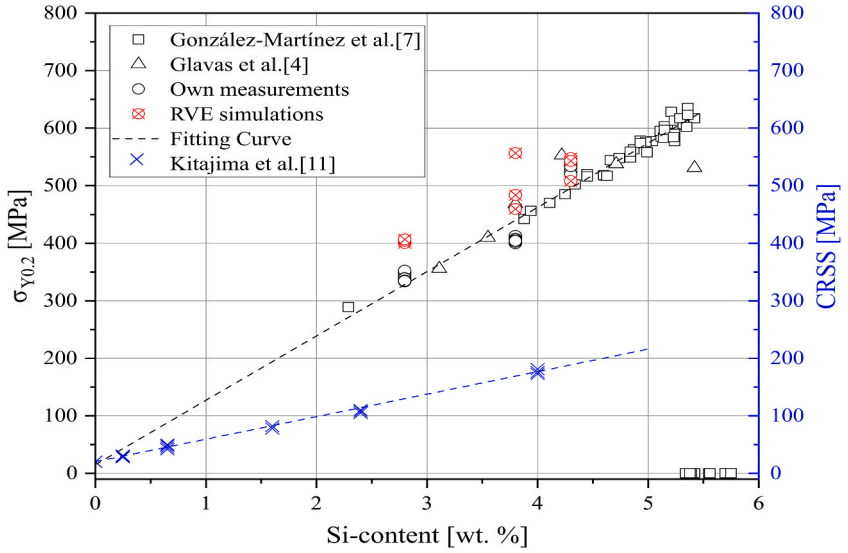

Fig. 14. Simulated values for $\sigma_{Y0.2}$ compared to values determined experimentally by means of macroscopic tensile tests and values of the CRSS of high-purity Fe–Si single crystals.

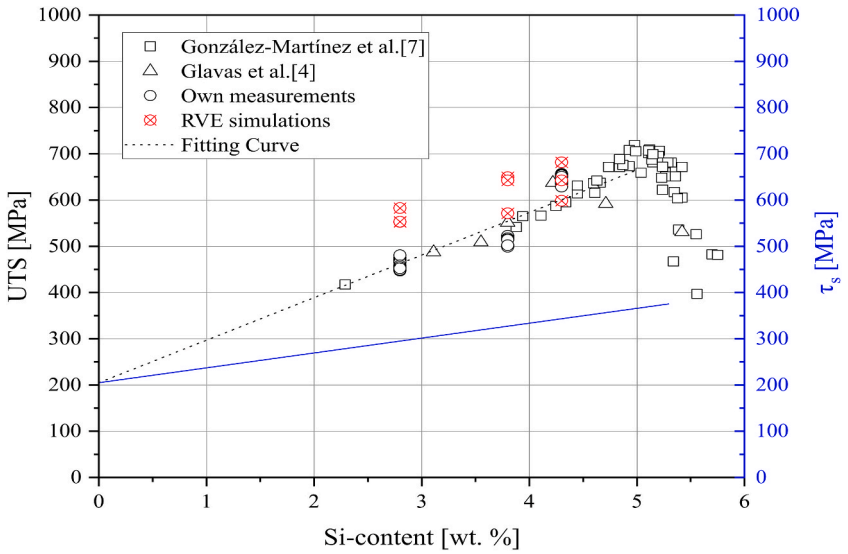

Fig. 15. Simulated values for the UTS compared to values determined experimentally by means of macroscopic tensile tests and assumed values for τ_s.

as calculated from the phase field simulation consistently exhibit lower values for the elongation at fracture and toughness (U) than the models with homogenized segregation profile.

Numerical and experimental results of the different RVEs are plotted together in Figs. 14–16. In Fig. 14 a comparison of the yield limits shows a good agreement of simulated values with the values obtained from tensile tests. The models of alloy MediumSi show a relatively large scatter in the simulated values for the 0.2 % offset yield limit, whereas the scatter for the other alloys is significantly lower. Comparing the tensile strengths shown in Fig. 15, larger deviations between simulated and experimentally determined values can be observed. The values for the ultimate tensile strength are overestimated by the models of the alloys LowSi and MediumSi. Good accuracy in prediction can be observed by comparing the simulated elongations at fracture with the experimental ones.

4. Discussion

The overall objective of this study was to investigate the effect of silicon micro-segregation on the mechanical properties under monotonic loading. In order to achieve this goal, samples of different alloy composition and different cooling rates were investigated

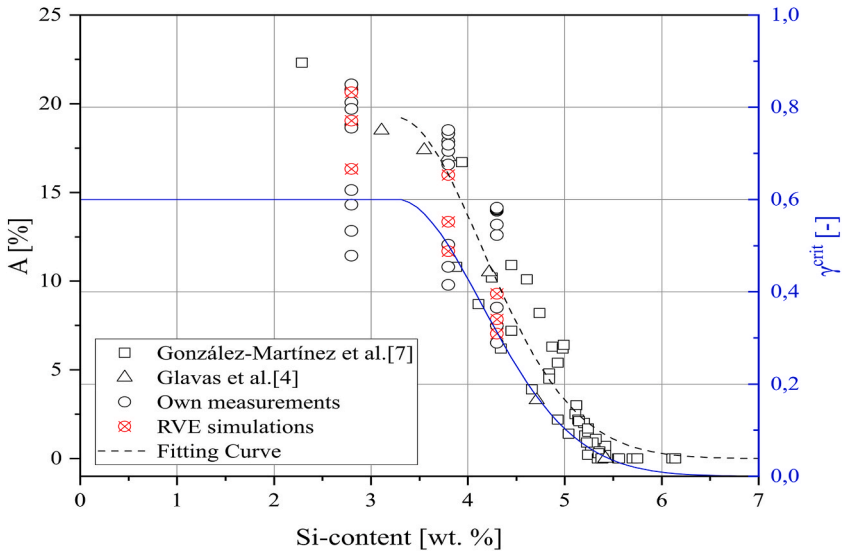

Fig. 16. Simulated values for the elongation at fracture compared to values determined experimentally by means of macroscopic tensile tests and assumed values for γ_{crit}.

using a coupled experimental and simulative approach.

4.1. Effect of silicon on deformation mechanisms

The objective of the in-situ investigation as well as the slip trace analysis was to verify whether the activation of slip in high silicon alloyed nodular cast iron changes due to the silicon content. The results showed that the majority of the slip traces were parallel to the {110} slip system. In only two cases, this parallelism could not be detected, which is attributed to high plastic deformation and the resulting reorientation of the crystal lattice. In order to assess the significance of these results, two major drawbacks of the method used must be mentioned. First, the method used does not provide a unique conclusion on the activation of slip systems during the deformation since the analysis is limited to the slip traces on the sample surface. Moreover, the probability of finding a parallel match increases with increasing number of slip planes in a slip system. However, the {110} slip planes are the elementary slip systems in pure ferrite according to Caillard [39,40]. Secondly, it must be taken into account that the presence of a free surface can influence the dislocation slip. According to a comparison of optical slip trace analysis with TEM images carried out by Weinberger et al. [13], the underlying dislocation structure determines the slip traces on the sample surface, but is not necessarily representative of the bulk plastic processes. However, a limitation to the {110} slip systems in the model is considered to be justified, since the majority of the slip traces showed a parallelism to these systems. Nevertheless, further investigation is of great interest for the continuation of this work. The in-situ tensile tests revealed that the deformation in the alloy with low silicon content is characterized by large amount of plasticity, which accumulates in highly stressed regions, e.g. graphite nodules. The accumulation of plastic deformation is particularly evident from the high topography differences, which can be observed in the colored BSE images given in Fig. 8. The presence of a large amount of accumulated plastic deformation shows the applicability of the damage model described in Section 2.3.2. The insitu analysis confirmed the results of Wittig et al. [8] who found a transition point at an overall amount of 4 wt% silicon, above which the shape of the slip traces changes from a wavy to an almost perfectly straight shape. This was attributed by Wittig et al. [8] to the presence of *B*2- and DO_3 superstructures and the formation of APB, which prevent dislocation cross-slip and therefore restrict the accumulation of plastic deformation. The transition point coincides with the global silicon content of the investigated materials, above which the elongation at fracture rapidly drops in macroscopic tensile tests (cf. Fig. 16). Accordingly, the global silicon content seems to be responsible for the drop in elongation at fracture and thus for the drop in toughness, rather than the presence of silicon segregation.

4.2. Effect of silicon and silicon segregation on mechanical properties under monotonous loading

The results of the micromechanical simulations show the effect of silicon segregation on the mechanical properties which is separated from other impact factors. All the models used were generated twice, once with the silicon profile as calculated by means of phase field simulations and once with a completely homogenized segregation profile. Comparing the results of both models showed that a homogenization of the silicon segregation leads to an increase in both the elongation at fracture and the toughness. An increase in yield limit and tensile strength can only be achieved to a negligible extent. The results can be justified by the following considerations.

- The negligible differences in 0.2 % offset yield limit and tensile strength can be explained by the linear dependence of the critical resolved shear and saturation stress on the local silicon content. Due to the volumetric averaging of the micromechanical stress and strain fields the impact of locally varying silicon contents vanishes. Based on this, the global silicon content, has the greatest effect on the yield limit, as well as the tensile strength. The comparison of the stress-strain curves in Fig. 11 indicates that differences between the models with homogenized silicon profile and phase-field segregation only become visible when damage is taken into account. Without damage, the stress strain curves of both models are almost the same, this is in agreement with the results obtained by Andriollo et al. [17].
- The larger variations in elongation at fracture and toughness result from the non-linear relationship between the critical amount of shear γ_{crit} and the local silicon content. The value of γ_{crit} determines the onset of damage based on the accumulation of plastic strain which leads to an earlier damage initiation in regions with elevated silicon content.
- However, the improvement in elongation at fracture and toughness is relatively low. Fig. 17 shows the cumulative distribution function of the silicon content in the ferritic matrix of the models LowSi-Y2, MediumSi-Y2 and HighSi-Y2. Based on these plots, the asymmetric shape of the silicon distribution can be clearly seen. As a results of the asymmetry, the maximum silicon content of the models differs only slightly from the global silicon content. Therefore, the critical amount of shear (γ_{crit}) of regions with maximum silicon content also differs only slightly from its value corresponding to the regions of the global silicon content. So it is rather the global silicon content that mainly influences the effective mechanical properties under monotonic loading. Fig. 13 also indicates that the largest deviations are caused by changes in the global silicon content.

Since the experiments were used to calibrate the missing model parameters (saturation stress τ_s and critical shear γ_{crit}), their good agreement with simulated data justifies the applied procedure. However, the finding is limited to the cooling rates of Y2 and Y4 casting specimens, while the predicted mechanical properties of casting specimens Cyl deviate from the experiments which can be understood from the size effect of the RVE.

Due to high computational efforts resulting from both the phase field and the crystal plasticity simulations, the chosen RVE size represents a compromise between computational effort and accuracy. Since the main objective of this work was to investigate the influence of silicon segregation on the effective mechanical properties under monotonic loading, the selected size of the RVE should be reasonable. However, the experimental results of Cyl show much larger graphite nodules compared to Y2 and Y4 leading to a strongly reduced measured elongation at fracture which is well known from literature [57]. A continuation of this work should also include the implementation of more complex damage formulations in order to increase the accuracy of the prediction and to improve the modeling of the damage initiation and evolution. This can be for example a Gurson-Tvergaard-Needleman model, which is capable of incorporating effects such as void nucleation, void growth and coalescence.

5. Conclusions

The overall objective of this study is to investigate the effect of silicon segregation on the effective mechanical properties of Si-DCI, especially on the toughness. Crystal plasticity simulations were performed on RVE generated by multi-phase field simulations. The main findings are summarized as follows:

- The effect of silicon segregation is only evident in the model when damage is taken into account. The yield limit, as well as the tensile strength are influenced to a negligible extent by the characteristics of the segregation profile, whereas the effect on elongation at fracture and toughness is higher.
- Under consideration of damage, a homogenization of the segregation profile has a positive effect on the elongation at fracture and toughness of the DCI alloy. However, the differences obtained are limited due to the asymmetric shape of the silicon distribution in the present microstructures.
- The global amount of silicon in DCI has the most significant impact on the effective mechanical properties under monotonic loading in both experiments and simulation.

Crucial for future work is a more sophisticated determination of the absent model parameters depending on the local silicon content. Micropillar compression tests offer a possibility to investigate regions with different silicon contents and to determine the

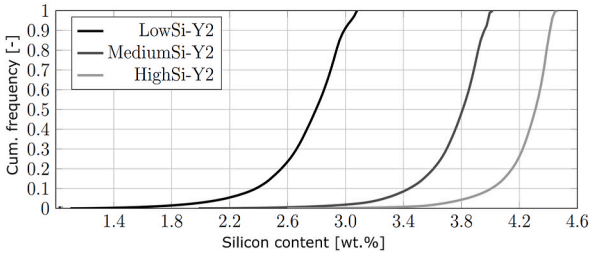

Fig. 17. Cumulative density plot of the silicon content soluted in the ferritic matrix of the RVE LowSi-Y2, MediumSi-Y2 and HighSi-Y2 from phase field simulation (dashed lines indicate the global silicon content in the corresponding models).

missing parameters. Furthermore, for a reliable determination of effective mechanical properties under monotonic load it is required to investigate the size effect of the models. In particular, more and larger RVEs are required to account for the effects of graphite and matrix microstructure in the model, which dominate the effective mechanical properties.

Data availability statement

Data will be made available on request.

CRediT authorship contribution statement

Lutz Horbach: Investigation, Methodology, Writing – original draft. **Christian Gebhardt:** Supervision, Writing – review & editing. **Jiali Zhang:** Methodology, Supervision, Writing – review & editing. **Betto David Joseph:** Investigation, Methodology, Writing – original draft. **Andreas Bührig-Polaczek:** Funding acquisition. **Christoph Broeckmann:** Funding acquisition.

Declaration of competing interest

The authors declare the following financial interests/personal relationships which may be considered as potential competing interests:Christoph Broeckmann and Andreas Bührig-Polaczek report financial support was provided by German Research Foundation.

Acknowledgements

The authors acknowledge funding by the Deutsche Forschungsgemeinschaft (DFG, German Research Foundation) within the project “Mechanisms of failure in solid solution strengthened spheroidal graphite cast iron” under grant no BR 1844/43-1 and BU 1072/47-1.

Appendix

Table 6
Polishing steps for the sample preparation

	1	2	3	4	5
Base	Hard silk				Synthetic cloth
Combound	Monocrystalline diamond				Aluminum oxide
Step	6 μm	3 μm	1 μm	0.25 μm	0.05 μm
Lubricant	Oil based				Water
Velocity	150 1/min				
Duration	1 min				
Repetitions	2–3				2

References

[1] BWE, Entwicklung von Größe und Durchmesser von Windenergieanlagen in Deutschland in den Jahren 2012 bis 2021, 2022. https://de.statista.com/statistik/daten/studie/1338775/umfrage/groesse-von-windenergieanlagen/.
[2] N.S. Tiedje, Solidification, processing and properties of ductile cast iron, Mater. Sci. Technol. 26 (5) (2010) 505–514, https://doi.org/10.1179/026708310X12668415533649.
[3] C. Gebhardt, T. Sedlatschek, A. Bezold, C. Broeckmann, Fullfield inverse identification of elasto-plastic model parameters for ductile cast iron, Mech. Mater. 162 (2021), 104056, https://doi.org/10.1016/j.mechmat.2021.104056.
[4] Z. Glavas, A. Strkalj, A. Stojakovic, The properties of silicon alloyed ferritic ductile irons, Metalurgija 2016 (55) (2016) 293–296.
[5] A. Alhussein, M. Risbet, A. Bastien, J.P. Chobaut, D. Balloy, J. Favergeon, Influence of silicon and addition elements on the mechanical behavior of ferritic ductile cast iron, Mater. Sci. Eng., A 605 (2014) 222–228, https://doi.org/10.1016/j.msea.2014.03.057.
[6] R. González-Martínez, U. de La Torre, A. Ebel, J. Lacaze, J. Sertucha, Effects of high silicon contents on graphite morphology and room temperature mechanical properties of as-cast ferritic ductile cast irons. part II – mechanical properties, Mater. Sci. Eng., A 712 (2018) 803–811, https://doi.org/10.1016/j.msea.2017.11.051.
[7] R. González-Martínez, U. de La Torre, J. Lacaze, J. Sertucha, Effects of high silicon contents on graphite morphology and room temperature mechanical properties of as-cast ferritic ductile cast irons. part I – microstructure, Mater. Sci. Eng., A 712 (2018) 794–802, https://doi.org/10.1016/j.msea.2017.11.050.
[8] J.E. Wittig, G. Frommeyer, Deformation and fracture behavior of rapidly solidified and annealed iron-silicon alloys, Metall. Mater. Trans. 39 (2) (2008) 252–265, https://doi.org/10.1007/s11661-0079436-7.
[9] D. Franzen, P. Weiß, B. Pustal, A. Bührig-Polaczek, Modification of silicon microsegregation in solid-solution-strengthened ductile iron by alloying with aluminum, Int. J. Metalcast. 100 (101) (2020) 70, https://doi.org/10.1007/s40962-020-00412-7.
[10] J. Eiken, E. Subasic, J. Lacaze, 3d phase-field computations of microsegregation in nodular cast iron compared to experimental data and calphad-based scheil-prediction, Materialia 9 (2020), 100538, https://doi.org/10.1016/j.mtla.2019.100538.
[11] K. Kitajima, Y. Aono, H. Abe, E. Kuramoto, Solid solution hardening and softening in iron alloy single crystals between 4.2 k and 300 k, Strength of Metals and Alloys (2) (1979) 965–970, https://doi.org/10.1016/B978-14832-8412-5.50161-2.

[12] K. Okazaki, Solid-solution hardening and softening in binary iron alloys, J. Mater. Sci. 31 (4) (1996) 1087–1099, https://doi.org/10.1007/BF00352911.
[13] C.R. Weinberger, B.L. Boyce, C.C. Battaile, Slip planes in bcc transition metals, Int. Mater. Rev. 58 (5) (2013) 296–314, https://doi.org/10.1179/1743280412Y.0000000015.
[14] C. Gebhardt, J. Nellessen, A. Bührig-Polaczek, C. Broeckmann, Influence of aluminum on fatigue strength of solution-strengthened nodular cast iron, Metals 11 (2) (2021) 311, https://doi.org/10.3390/met11020311.
[15] M. Endo, T. Matsuo, A practical method for fatigue limit prediction in ductile cast irons, Fatig. Fract. Eng. Mater. Struct. 211 (4) (2019) 628, https://doi.org/10.1111/ffe.13086.
[16] A.K. Kasvayee, E. Ghassemali, I.L. Svensson, J. Olofsson, A.E.W. Jarfors, Characterization and modeling of the mechanical behavior of high silicon ductile iron, Mater. Sci. Eng., A 708 (2017) 159–170, https://doi.org/10.1016/j.msea.2017.09.115.
[17] T. Andriollo, N. Tiedje, J. Hattel, Distance map based micromechanical analysis of the impact of matrix heterogeneities on the yield stress of nodular cast iron, Mech. Mater. 148 (2020), 103414, https://doi.org/10.1016/j.mechmat.2020.103414.
[18] F. Roters, P. Eisenlohr, L. Hantcherli, D.D. Tjahjanto, T.R. Bieler, D. Raabe, Overview of constitutive laws, kinematics, homogenization and multiscale methods in crystal plasticity finite-element modeling: theory, experiments, applications, Acta Mater. 58 (4) (2010) 1152–1211, https://doi.org/10.1016/j.actamat.2009.10.058.
[19] F. Roters, M. Diehl, P. Shanthraj, P. Eisenlohr, C. Reuber, S.L. Wong, T. Maiti, A. Ebrahimi, T. Hochrainer, H.-O. Fabritius, S. Nikolov, M. Friák, N. Fujita, N. Grilli, K. Janssens, N. Jia, P. Kok, D. Ma, F. Meier, E. Werner, M. Stricker, D. Weygand, D. Raabe, Damask – the düsseldorf advanced material simulation kit for modeling multi-physics crystal plasticity, thermal, and damage phenomena from the single crystal up to the component scale, Comput. Mater. Sci. 158 (2019) 420–478, https://doi.org/10.1016/j.commatsci.2018.04.030.
[20] W. Liu, J. Lian, N. Aravas, S. Münstermann, A strategy for synthetic microstructure generation and crystal plasticity parameter calibration of fine-grain-structured dual-phase steel, Int. J. Plast. 126 (2020), 102614, https://doi.org/10.1016/j.ijplas.2019.10.002.
[21] H.J. Bong, H. Lim, M.-G. Lee, D.T. Fullwood, E.R. Homer, R.H. Wagoner, An rve procedure for micromechanical prediction of mechanical behavior of dual-phase steel, Mater. Sci. Eng., A 695 (2017) 101–111, https://doi.org/10.1016/j.msea.2017.04.032.
[22] V. Balobanov, M. Lindroos, T. Andersson, A. Laukkanen, Crystal plasticity modeling of grey cast irons under tension, compression and fatigue loadings, Crystals 12 (2) (2022) 238, https://doi.org/10.3390/cryst12020238.
[23] ACCESS e.V., Micress, 2022. www.micress.de.
[24] J. Eiken, B. Böttger, I. Steinbach, Multiphase-field approach for multicomponent alloys with extrapolation scheme for numerical application, Phys. Rev. E: Stat., Nonlinear, Soft Matter Phys. 73 (6 Pt 2) (2006), 066122, https://doi.org/10.1103/PhysRevE.73.066122.
[25] M. Chen, Q. Du, R. Shi, H. Fu, Z. Liu, J. Xie, Phase field simulation of microstructure evolution and process optimization during homogenization of additively manufactured inconel 718 alloy, Frontiers in Materials 9 (2022), https://doi.org/10.3389/fmats.2022.1043249.
[26] D. Agius, P. O'Toole, C. Wallbrink, Z. Sterjovski, C.-H. Wang, G.B. Schaffer, Integrating phase field and crystal plasticity finite element models for simulations of titanium alloy ti-5553, J. Phys.: Materials 4 (4) (2021), 044014, https://doi.org/10.1088/2515-7639/ac194f.
[27] T. Pinomaa, M. Lindroos, M. Walbrühl, N. Provatas, A. Laukkanen, The significance of spatial length scales and solute segregation in strengthening rapid solidification microstructures of 316l stainless steel, Acta Mater. 184 (2020) 1–16, https://doi.org/10.1016/j.actamat.2019.10.044.
[28] C.C. Tasan, J. Hoefnagels, M. Diehl, D. Yan, F. Roters, D. Raabe, Strain localization and damage in dual phase steels investigated by coupled in-situ deformation experiments and crystal plasticity simulations, Int. J. Plast. 63 (2014) 198–210, https://doi.org/10.1016/j.ijplas.2014.06.004.
[29] C. Zambaldi, C. Zehnder, D. Raabe, Orientation dependent deformation by slip and twinning in magnesium during single crystal indentation, Acta Mater. 91 (2015) 267–288, https://doi.org/10.1016/j.actamat.2015.01.046.
[30] A.K. Kasvayee, K. Salomonsson, E. Ghassemali, A.E.W. Jarfors, Microstructural strain distribution in ductile iron; comparison between finite element simulation and digital image correlation measurements, Mater. Sci. Eng., A 655 (2016) 27–35, https://doi.org/10.1016/j.msea.2015.12.056.
[31] C. Du, F. Maresca, M. Geers, J. Hoefnagels, Ferrite slip system activation investigated by uniaxial micro-tensile tests and simulations, Acta Mater. 146 (2018) 314–327, https://doi.org/10.1016/j.actamat.2017.12.054.
[32] DIN Deutsches Institut für Normung e. V., ISO/DIN 945-4: Test Method for Evaluating Nodularity in Spheroidal Graphite Cast Irons, 2022.
[33] E04 Committee, Test Method for Determining Nodularity and Nodule Count in Ductile Iron Using Image Analysis. doi:10.1520/E2567-16A..
[34] DIN Deutsches Institut für Normung e. V., DIN 50125:2016-12, Prüfung Metallischer Werkstoffe - Zugproben: Zugproben, 2022, https://doi.org/10.31030/2577390.
[35] DIN Deutsches Institut für Normung e. V., DIN EN ISO 6506-1:2015-02, Metallische Werkstoffe - Härteprüfung nach Brinell - Teil 1: Prüfverfahren (ISO 6506-1:2014); Deutsche Fassung EN ISO 6506-1:2014: Deutsche Fassung. doi:10.31030/2146324..
[36] T.R. Bieler, P. Eisenlohr, F. Roters, D. Kumar, D.E. Mason, M.A. Crimp, D. Raabe, The role of heterogeneous deformation on damage nucleation at grain boundaries in single phase metals, Int. J. Plast. 25 (9) (2009) 1655–1683, https://doi.org/10.1016/j.ijplas.2008.09.002.
[37] B.A. Simkin, B.C. Ng, T.R. Bieler, M.A. Crimp, D.E. Mason, Orientation determination and defect analysis in the near-cubic intermetallic γ-TiAl using SACP, ECCI, and EBSD, Intermetallics 11 (3) (2003) 215–223, https://doi.org/10.1016/S0966-9795(02)00236-4.
[38] W.A. Spitzig, A.S. Keh, Orientation and temperature dependence of slip in iron single crystals, Metall. Mater. Trans. B 1 (10) (1970), https://doi.org/10.1007/BF03037811.
[39] D. Caillard, Kinetics of dislocations in pure Fe. part I. in situ straining experiments at room temperature, Acta Mater. 58 (9) (2010) 3493–3503, https://doi.org/10.1016/j.actamat.2010.02.023.
[40] D. Caillard, Kinetics of dislocations in pure Fe. part II. in situ straining experiments at low temperature, Acta Mater. 58 (9) (2010) 3504–3515, https://doi.org/10.1016/j.actamat.2010.02.024.
[41] Thermo-Calc Software, Thermo-calc, 2022. www.thermocalc.de.
[42] J. Eiken, M. Apel, S.-M. Liang, R. Schmid-Fetzer, Impact of P and Sr on solidification sequence and morphology of hypoeutectic Al–Si alloys: combined thermodynamic computation and phase-field simulation, Acta Mater. 98 (2015) 152–163, https://doi.org/10.1016/j.actamat.2015.06.056.
[43] J.W. Hutchinson, Bounds and self-consistent estimates for creep of polycrystalline materials, Proceedings of the Royal Society of London. A. Mathematical and Physical Sciences 348 (1652) (1976) 101–127, https://doi.org/10.1098/rspa.1976.0027.
[44] T. Andriollo, J. Hattel, On the isotropic elastic constants of graphite nodules in ductile cast iron: analytical and numerical micromechanical investigations, Mech. Mater. 96 (2016) 138–150, https://doi.org/10.1016/j.mechmat.2016.02.007.
[45] T. Andriollo, J. Thorborg, J. Hattel, Modeling the elastic behavior of ductile cast iron including anisotropy in the graphite nodules, Int. J. Solid Struct. 100–101 (2016) 523–535, https://doi.org/10.1016/j.ijsolstr.2016.09.023.
[46] F. Qayyum, M. Umar, S. Guk, M. Schmidtchen, R. Kawalla, U. Prahl, Effect of the 3rd dimension within the representative volume element (RVE) on damage initiation and propagation during full-phase numerical simulations of single and multi-phase steels, Materials 14 (1) (2020), https://doi.org/10.3390/ma14010042.
[47] F. Qayyum, S. Guk, U. Prahl, Studying the damage evolution and the micro-mechanical response of X8CrMnNi16-6-6 trip steel matrix and 10% zirconia particle composite using a calibrated physics and crystalplasticity-based numerical simulation model, Crystals 11 (7) (2021) 759, https://doi.org/10.3390/cryst11070759.
[48] V. Di Cocco, F. Iacoviello, M. Cavallini, Damaging micromechanisms characterization of a ferritic ductile cast iron, Eng. Fract. Mech. 77 (11) (2010) 2016–2023, https://doi.org/10.1016/j.engfracmech.2010.03.037.
[49] M. Warmuzek, A. Polkowska, Micromechanism of damage of the graphite spheroid in the nodular cast iron during static tensile test, Journal of Manufacturing and Materials Processing 4 (1) (2020) 22, https://doi.org/10.3390/jmmp4010022.
[50] N. Bonora, A. Ruggiero, Micromechanical modeling of ductile cast iron incorporating damage. part i: ferritic ductile cast iron, Int. J. Solid Struct. 42 (5–6) (2005) 1401–1424, https://doi.org/10.1016/j.ijsolstr.2004.07.025.

[51] D.O. Fernandino, A.P. Cisilino, S. Toro, P.J. Sanchez, Multi-scale analysis of the early damage mechanics of ferritized ductile iron, Int. J. Fract. 207 (1) (2017) 1–26, https://doi.org/10.1007/s10704017-0215-1.
[52] T. Andriollo, Y. Zhang, S. Fæster, J. Thorborg, J. Hattel, Impact of micro-scale residual stress on in-situ tensile testing of ductile cast iron: digital volume correlation vs. model with fully resolved microstructure vs. periodic unit cell, J. Mech. Phys. Solid. 125 (2019) 714–735, https://doi.org/10.1016/j.jmps.2019.01.021.
[53] J. Cho, Voronoi diagram and microstructure of weldment, J. Mech. Sci. Technol. 29 (1) (2015) 371–374, https://doi.org/10.1007/s12206-014-1244-6.
[54] Z. Fan, Y. Wu, X. Zhao, Y. Lu, Simulation of polycrystalline structure with voronoi diagram in laguerre geometry based on random closed packing of spheres, Comput. Mater. Sci. 29 (3) (2004) 301–308, https://doi.org/10.1016/j.commatsci.2003.10.006.
[55] S. Katani, S. Ziaei-Rad, N. Nouri, N. Saeidi, J. Kadkhodapour, N. Torabian, S. Schmauder, Microstructure modelling of dual-phase steel using sem micrographs and voronoi polycrystal models, Metallography, Microstructure, and Analysis 2 (3) (2013) 156–169, https://doi.org/10.1007/s13632013-0075-7.
[56] W.C. Leslie, Iron and its dilute substitutional solid solutions, Metall. Mater. Trans. B 3 (1) (1972) 5–26, https://doi.org/10.1007/BF02680580.
[57] D. Franzen, B. Pustal, A. Bührig-Polaczek, Influence of graphitephase parameters on the mechanical properties of high-silicon ductile iron, Int. J. Metalcast. 17 (1) (2023) 4–21, https://doi.org/10.1007/s40962-022-00761-5.